HIGH TEMPERATURE SOLID PARTICLE EROSION IN A MELT-INFILTRATED SIC/SIC CERAMIC MATRIX COMPOSITE

Michael J. Presby

NASA Glenn Research Center, Cleveland OH 44135
Email: michael.presby@nasa.gov

ABSTRACT

Ceramic matrix composites (CMCs) are an enabling propulsion material system that offer weight benefits over current Ni-based superalloys, and have higher temperature capabilities that can reduce cooling requirements. Incorporating CMCs into the hot section of gas-turbine engines therefore leads to an increase in engine efficiency. While significant advancements have been made, challenges still remain for current and next-generation gas-turbines; particularly when operating in dust-laden or erosive environments. Solid particles entrained in the gas flow can impact engine hardware resulting in localized damage and material removal due to repeated, cumulative impacts. In this study, the erosion behavior of a melt-infiltrated (MI) silicon carbide fiber-reinforced silicon carbide (SiC/SiC) CMC is investigated at high temperature (1,200 °C) in a simulated combustion environment using 150 µm alumina particles as erodent. Particle impact velocities ranged from 100 to 200 m/s and the angle of impingement varied from 30° to 90°. Erosion testing was also performed on α-SiC to elucidate similarities and differences in the erosion response of the composite compared to that of a monolithic ceramic. Scanning electron microscopy (SEM) was used to study the post-erosion damage morphology and the governing mechanisms of material removal.

[Keywords: Ceramic matrix composites (CMCs), solid particle erosion, high temperature, burner rig].

INTRODUCTION

Advanced hot-section material systems are a critical technology for the advancement of gas turbines, particularly as the aero industry pushes for more efficient and powerful engines. Silicon carbide fiber-reinforced silicon carbide (SiC/SiC) CMCs are considered a key material system for hot-section hardware due to their low density, high strength, and toughness. These characteristics enable improvements in engine efficiency [1].

While CMCs possess many favorable properties and characteristics, significant design challenges still exist for CMC components, especially in gas-turbine engines operating in dust-laden, erosive environments. The damage resulting from a repetitive, cumulative impact of solid erosive particles can cause significant material removal which leads to reduced structural integrity and decreased engine performance. As a result, it is important to characterize and develop a fundamental understanding of the erosion processes and damage mechanisms in gas-turbine grade CMCs subject to erosive environments.

In service, engine hardware can be subject to a wide range of erosive conditions that will be dependent upon temperature, particle type/composition, velocity, angle of impingement, etc. Recently, several studies have been

performed to begin characterizing the erosion response of gas-turbine grade CMCs at ambient temperature [2, 3, 4]. These studies showed that CMCs can be susceptible to significant material removal and that the corresponding damage mechanisms are not easily elucidated due to the complex architecture/microstructure of these composite systems. Nevertheless, bulk material properties such as modulus, density, and apparent matrix hardness were used to correlate the observed erosion responses. CMCs that possessed higher modulus, density, and hardness exhibited greater erosion resistance.

A recent investigation [3] into the erosion response of an MI SiC/SiC CMC at ambient temperature using garnet erodent analyzed the effect of particle velocity and particle size. The findings showed good correlation with particle kinetic energy being a controlling variable of the overall erosion rate. Investigation of the post-erosion damage morphology showed a localized tunneling effect in regions containing defects (i.e. porosity) further showing the importance of achieving a high-density composite material. Lastly, any particular sign of a predominant cracking system responsible for material removal, such as lateral cracking, was not easily identifiable due to the complexity of the material system.

The erosion behavior of CMCs in gas-turbine environments is governed by various factors related to engine operating conditions and material properties. Consequently, it is important to continue to assess the erosion behavior of CMCs under various erosion conditions, particularly those similar to what will be encountered in service. As such, the objective of the current work is to systematically investigate the erosion behavior of an MI SiC/SiC CMC at elevated temperature in a simulated combustion environment. Particle velocities are varied from 100 to 200 m/s, and a range of particle impingement angles from 30° to 90° are evaluated. Scanning electron microscopy (SEM) is utilized post-erosion to understand the predominate damage mechanisms. The erosion behavior of the MI SiC/SiC CMC is also compared to that of a monolithic, α-SiC ceramic material.

EXPERIMENTAL PROCEDURE

Target Material Systems

The CMC material system used in this work was a Hi-Nicalon^{TM} Type S (HNS), boron nitride (BN)-interphase, slurry-cast melt-infiltrated (MI) SiC matrix composite. The CMC panel consisted of eight plies of 5-harness satin-weave fabric oriented in the 0° and 90° directions with an as-received panel thickness of 2.1 mm. The bulk density of the CMC material was determined to be 2.58 ± 0.06 g/cm^3.

The monolithic SiC material used in this work was α-SiC (Hexoloy® SA). The as-received thickness was 3.0 mm. The bulk density of the α-SiC was determined to be 3.10 ± 0.02 g/cm^3.

All erosion samples (CMC and α-SiC) were machined into 25.4 mm (1.0 inch) diameter disks.

Erosion Facility and Erosion Testing

Erosion testing was performed using a high velocity burner rig with instrumented erosion capability. The erosion burner rig has been described in detail elsewhere [5, 6, 7], but an overview is described here briefly.

The erosion burner rig facility is a modified NASA Glenn Mach 0.3 to Mach 1.0 burner rig [8] that operates on Jet-A fuel and preheated air. A screw-driven powder feeder (HA 5000F-SA, Hardface Alloys, Inc.) delivers the erodent through a feed line that injects into the burner chamber where the erodent passes through a 19 mm diameter exit

nozzle, and is accelerated downstream through a 19 mm diameter, 305 mm long unattached duct. A high temperature, spring-loaded, clamshell fixture is used to hold the sample during testing. The clamshell fixture is placed at the end of the duct with a standoff distance between the duct exit and the center of the sample set to 30 mm. A photograph of the burner exit nozzle, the unattached duct, and the clamshell sample fixture is shown in Fig. 1(a), and a schematic of the burner rig placed before the duct is displayed in Fig. 1(b). Note that the burner rig can be pivoted on and off the sample for heating and cooling, and is displayed in the off, or cooling position in Fig. 1(a). The test samples were heated to 1,200 °C (2,192 °F) as measured by a Williamson Corporation two-color pyrometer. Uniform heating of the sample surface was verified with a FLIR A655sc thermal imaging camera where the typical temperature distribution across the sample was within 10 °C as shown in Fig. 2(a) and Fig. 2(b).

After heating, the samples were then exposed to 150 μm mean diameter alumina (Al_2O_3) particles. Alumina was chosen since it is readily available and shown to produce 'erosion scars' or damage similar to that observed in engine hardware [6, 7, 9]. The particles were injected into the burner rig at a rate of 2 g/min. Three different particle velocities were used; 100, 150, and 200 m/s. The angle of particle impingement was varied between 30° and 90° for the 100 m/s particle velocity at increments of 15° (i.e. 30°, 45°, 60°, 75°, and 90°).

Particle velocities were measured using the double disk velocimetry method [10, 11, 12], and adapted for use at elevated temperatures by fabricating the disks out of Inconel® 601. A schematic of the double disk is displayed in Figure 3. In this method, two disks rotate on a common axis that is parallel to the erosive particle stream. The first disk (Disk 1), contains a slit that allows the particles to pass through and impinge on the second disk (Disk 2) where an erosion scar is produced. For a fixed angular velocity, ω, and a fixed separation distance between the two disks, L, the erosion scar on Disk 2 relative to the slit on Disk 1 is related to the particle velocity, v, based on the angle, θ. The following relationship is used to determine particle velocity:

$$v = \frac{\omega L}{\theta} \tag{1}$$

The double disk method was improved by rotating the disks clockwise to obtain one erosion scar, and then counterclockwise to obtain a second erosion scar; thus doubling the distance, 2θ, between the scars. This procedure helps to improve the accuracy of the velocity measurements as described by Wiederhorn and Hockey [12].

For erosion testing, the samples were subject to multiple exposures where the sample mass was measured before and after each exposure. The sample mass was measured using a scale with a precision of 0.01 mg. The steady-state erosion rate was determined via a regression fit in the linear region of the cumulative mass loss versus cumulative mass erodent curve. The last six data points of each curve were used for the regression analysis.

Lastly, the samples were characterized using SEM to assess the damage morphology from the eroded surfaces.

RESULTS AND DISCUSSION

Effect of Particle Velocity

Typical cumulative mass loss versus cumulative mass erodent curves are shown in Fig. 4 for the MI SiC/SiC CMC and α-SiC at normal (90°) impingement for the three velocities tested; 100, 150, and 200 m/s. First, a well-

defined linear region (representing steady-state erosion condition) is observed for both materials after an initial, non-linear, transient region at each velocity. For the MI SiC/SiC, this initial transient is generally represented by an initial sharp increase (high slope) in mass loss at low erodent followed by a decrease in slope until steady-state is achieved. This implies that the required cracking, or damage responsible for material removal occurs early in the erosion process under these conditions.

The opposite behavior is observed for the α-SiC where an incubation period (little to no change in mass) followed by a gradual increase in slope is observed prior to reaching steady-state. As a result, a greater amount of erodent was required to reach steady-state conditions compared to the MI SiC/SiC. This suggests that there is a greater period for which the required build-up of surface, or subsurface, damage exists prior to reaching steady-state in the α-SiC. Similar weight loss transients, or incubation periods, have been reported by other researchers for SiC-based ceramics eroded with alumina particles [13, 14].

It is also evident from the cumulative mass loss versus cumulative mass erodent curves in Fig. 4 that an increase in mass loss and steady-state erosion rate is observed as particle velocity increases from 100 to 200 m/s. Figure 5 shows the steady-state erosion rate as a function of particle velocity. Note that the steady-state erosion rate shown in Fig. 5 is represented as volume loss [mm^3] per gram of erodent to better compare the steady-state erosion rates since the materials have different densities. The bulk densities reported earlier in the Experimental Procedure section were used to convert from mass to volume loss.

Both the MI SiC/SiC and α-SiC exhibit a power law dependence on the steady-state erosion rate, E with respect to particle velocity, v, of the form:

$$E = \varphi v^n \tag{2}$$

where $\varphi = 6.5 \times 10^{-5}$ and $n = 2.2$ for the MI SiC/SiC and $\varphi = 1.65 \times 10^{-7}$ and $n = 2.4$ for the α-SiC. The MI SiC/SiC exhibits an erosion rate that is approximately two orders of magnitude higher than α-SiC under the same conditions. This is consistent with previous work at room temperature using garnet erodent [2, 3]. Furthermore, both materials exhibit a velocity exponent, $n > 2$. This is common for many brittle materials subject to solid particle erosion where the velocity exponent typically ranges from 2 to 4 [12, 13, 15]. A quasi-static indentation fracture analysis for sharp particle impact predicts a velocity exponent (dependent upon assumptions used within the analysis) of 2.33 [16] or 2.44 [17] for lateral cracking dominated material removal, while a dynamic analysis predicts a velocity exponent of 3.17 [18]. Based on the conditions present in this study, both materials exhibit a velocity dependence closer to that of the quasi-static analyses.

Effect of Particle Impingement Angle

The effect of particle impingement angle was further evaluated since particles will impinge components over a wide range of angles during service. Exemplary cumulative mass loss versus cumulative mass erodent curves for the various impingement angles are shown in Fig. 6. For the MI SiC/SiC, a higher initial slope is observed prior to gradually decreasing to steady-state for all impingement angles. Conversely, little to no change in mass followed by a gradual increase to steady-state is observed for the α-SiC.

Assuming the erosion process at all impingement angles is controlled by brittle fracture, it has been suggested that the erosion response at lower (oblique) angles would be controlled by the indenting (normal) component of the particle velocity, $v \sin \alpha$ where α is the impingement angle [19, 20]. This would imply that

$$E \propto (v \sin \alpha)^n \tag{3}$$

where n is the velocity exponent at normal (90°) impingement.

Figure 7(a) and (b) plots the normalized steady-state erosion rate, E^* as a function of impingement angle for the MI SiC/SiC and α-SiC, respectively. The $\sin^n \alpha$ law for brittle controlled fracture where $n = 2.2$ for the MI SiC/SiC and $n = 2.4$ for the α-SiC, as experimentally determined from normal impingement, are also included. As shown in Fig. 7, both materials exhibit a maximum erosion rate at 90° and exhibit a general decrease in erosion rate as the impingement angle decreases. The trend in decreasing erosion rate as impingement angle decreases is in reasonable agreement with that predicted by the $\sin^n \alpha$ law for $\alpha \geq 60°$. As α decreases below 60°, the erosion rate becomes increasingly underpredicted. This suggests that there may be a change in mechanism as α decreases; namely an increasing contribution of the tangential component of velocity (defined here as the velocity component parallel to the sample surface, *v cos α*) which may indicate a larger contribution of plastic deformation.

Erosion Damage Morphology

Figure 8 shows the steady-state erosion surfaces for the MI SiC/SiC for 90° and 30° impingement angles at a particle velocity of 100 m/s. For 90° particle impingement, Fig. 8(a) shows the resultant erosion damage in a matrix-rich region where it is evident that material removal primarily occurs via brittle fracture. Transitioning to a fiber-rich region displayed in Fig. 8(b), extensive fiber breakage is observed suggesting that the fibers are highly susceptible to fracture and removal upon impact. At the lower impingement angle of 30°, shown in Fig. 8(c), the erosion surface morphology is characterized more by small grooves, or wear scars, that is representative of material removal occurring through a plastic, or ductile ploughing process. Extensive fiber damage is still observed at the lower impingement angle as evident from Fig. 8(d).

Figure 9 shows the resulting damage observed in the α-SiC for particle impingement angle of 90° at 200 m/s, and at 45° for 100 m/s. For 90° impingement, Fig. 9(a), material removal due to brittle fracture (lateral cracking) is evident. For 45° particle impingement, Fig. 9(b), an overall increase in plastic deformation is observed along with wear scars representing the ploughing and sliding of the particle along the surface that are similar to the observations for the MI SiC/SiC. Note the differences in scale of the apparent damage present in Fig. 8 and Fig. 9 that further highlight that the α-SiC is more resistant to damage upon impact.

This change in apparent mechanism from brittle-dominated material removal at higher impingement angles to a more ductile, ploughing process at lower impingement angles has been reported in other ceramic materials at ambient and elevated temperatures [13, 19, 20, 21, 22]. The increasing contribution of a ductile mode to the erosion process also supports the underprediction of the $\sin^n \alpha$ (Eq. (3) and Fig. 7) relationship as α decreases since the tangential component of velocity becomes non-negligible.

Isolated Impact Events in MI SiC/SiC

Due to the inherently more complex microstructure/architecture of the MI SiC/SiC, some samples were subject to low levels of erodent (~0.1 g) in hope to better elucidate the material removal mechanisms in the composite. By using a small dose of erodent, isolated areas of damage were often discernable. Figure 10 shows isolated impact events for 90° and 30° at 100 m/s in a matrix-rich region of the MI SiC/SiC. From Fig. 10(a), it is evident that material removal occurs via lateral cracking where the lateral cracks form beneath the impact site, extend, and curve up to intersect the surface resulting in chipping of the material. Figure 10(b) further highlights the visible grooves produced by the ploughing action of the particles at the lower impingement angle of 30°. Moreover, evidence of lateral cracking adjacent to the grooves implies that both brittle (lateral cracking), and ductile (ploughing) modes are operative at lower impingement angles and act jointly to remove material. This further validates the increasing contribution of the tangential velocity component as the impingement angle decreases.

For isolated impact events in close proximity to fibers, as shown in Fig. 11, regions of exposed, but intact, fibers are observed. The phenomenon is a result of a loss of matrix material where cracking occurred along the fiber-matrix interface. As shown in the SEM images in Fig. 11, this 'weak' interface can result in the exposure of large portions of fibers when subjected to erosion damage. Given that erosion is a cumulative event, debonded matrix material is easily removed and the exposed fibers are susceptible to fracture and removal upon successive particle impacts. In other fiber-reinforced composite material systems, the strength of the fiber-matrix interface has been shown to be an important parameter where mechanically weak interfaces are generally detrimental to erosion resistance [23, 24, 25]. While additional work is certainly warranted in understanding the effect of interfacial properties and toughness on the overall erosion response in the MI SiC/SiC, the fiber-matrix interface appears to be preferential for crack initiation and crack propagation early on in the erosion process.

CONCLUSIONS

Solid particle erosion is a complex phenomenon that can cause detrimental effects to engine hardware. The complexity is further increased in composite materials, such as CMCs, due to local variations in material, and properties derived from their architectural configurations. As such, continued characterization of the erosion processes in CMCs is required and should involve interdisciplinary approaches in experimental characterization, modeling, and simulation. While continued evaluation is needed, several important results have been presented in this study. Given the erosion conditions used in this work, the MI SiC/SiC exhibited an initial sharp increase in mass loss followed by a gradual decrease to steady-state. This was in contrast to the monolithic α-SiC where an incubation period with little to no change in mass was observed early on in the erosion process. Both the MI SiC/SiC and α-SiC exhibited power law dependencies on the steady-state erosion rate with respect to particle velocity where the MI SiC/SiC was approximately two orders of magnitude less resistant as compared to the monolithic α-SiC. The velocity exponents were in relative agreement with that predicted by quasi-static erosion analyses of indentation fracture where lateral cracking is the dominant material removal mechanism.

Analysis of the erosion damage through SEM showed lateral cracking as an operative mechanism for material removal in both the MI SiC/SiC and α-SiC. The weak, fiber-matrix interface in the MI SiC/SiC appeared to be preferential for crack propagation resulting in ejected matrix material even at a low dose of erodent, which exposed

underlying fibers and fiber tows. Fiber damage was extensive under steady-state conditions suggesting that the fibers are easily fractured and removed upon particle impact.

Lastly, a plastic ploughing process played an increasing role in the erosion behavior in both the MI SiC/SiC and α-SiC at lower impingement angles suggesting a non-negligible contribution of the tangential component of velocity.

ACKNOWLEDGEMENTS

The author is grateful to Michael Cuy for assistance in the experimental setup of the erosion burner rig facility, Pete Bonacuse and Wayne Jennings for assistance with SEM, and Bryan Harder for insightful discussion and scientific input. The NASA Aeronautics Research Mission Directorate (ARMD) Transformational Tools and Technologies (TTT) Project supported this work.

REFERENCES

[1] F. Zok, "Ceramic-Matrix Composites Enable Revolutionary Gains in Turbine Engine Efficiency," *American Ceramic Society Bulletin,* vol. 95, no. 5, pp. 22-28, 2016.

[2] N. Kedir, C. Gong, L. Sanchez, M. J. Presby, S. Kane, D. C. Faucett and S. R. Choi, "Erosion in Gas-Turbine Grade Ceramic Matrix Composites," *Journal of Engineering for Gas Turbines and Power,* vol. 141, no. 1, pp. 011019-1-9, 2019.

[3] M. J. Presby, C. Gong, S. Kane, N. Kedir, A. Stanley, D. C. Faucett and S. R. Choi, "Erosion in a Melt-Infiltrated SiC/SiC Ceramic Matrix Composite," *Journal of Engineering for Gas Turbines and Power,* vol. 142, no. 4, pp. 041009-1-9, 2020.

[4] M. J. Presby, N. Kedir, L. J. Sanchez, C. Gong, D. C. Faucett, S. R. Choi and G. N. Morscher, "Erosion Behavior in a Gas Turbine Grade Oxide/Oxide Ceramic Matrix Composite," in *Proceedings of the 42nd International Conference on Advanced Ceramics and Composites: Ceramic Engineering and Science Proceedings*, 2019.

[5] M. A. Kuczmarski, R. A. Miller and D. Zhu, "CFD-Guided Development of Test Rigs for Studying Erosion and Large-Particle Damage of Thermal Barrier Coatings," *Modelling and Simulation in Engineering,* vol. 2011.

[6] R. Miller and M. Kuczmarski, "Burner Rig for Small Particle Erosion Testing of Thermal Barrier Coatings," *Journal of Testing and Evaluation,* vol. 42, no. 3, pp. 648-658, 2014.

[7] R. A. Miller, M. A. Kuczmarski and D. Zhu, "Burner Rig with an Unattached Duct for Evaluating the Erosion Resistance of Thermal Barrier Coatings," NASA/TM – 2011-217008, 2011.

[8] D. S. Fox, R. A. Miller, D. Zhu, M. Perez, M. D. Cuy and R. C. Robinson, "Mach 0.3 Burner Rig Facility at the NASA Glenn Materials Research Laboratory," NASA/TM – 2011-216986, 2011.

[9] R. W. Bruce, "Development of 1232°C (2250°F) Erosion and Impact Tests for Thermal Barrier Coatings," *Tribology Transactions,* vol. 41, no. 4, pp. 399-410, 1998.

[10] A. W. Ruff and L. K. Ives, "Measurement of Solid Particle Velocity in Erosive Wear," *Wear,* vol. 35, pp. 195-199, 1975.

[11] A. Stevenson and I. Hutchings, "Scaling Laws for Particle Velocity in the Gas-Blast Erosion Test," *Wear,* Vols. 181-183, pp. 56-62, 1995.

[12] S. M. Wiederhorn and B. J. Hockey, "Effect of Material Parameters on the Erosion Resistance of Brittle Materials," *Journal of Materials Science,* vol. 18, pp. 766-780, 1983.

[13] J. L. Routbort, R. O. Scattergood and A. P. L. Turner, "Erosion of Reaction-Bonded SiC," *Wear,* vol. 59, no. 2, pp. 363-375, 1980.

[14] S. K. Sharma, B. V. M. Kumar, K.-Y. Lim, Y.-W. Kim and S. K. Nath, "Erosion Behavior of SiC-WC Composites," *Ceramics International,* vol. 40, no. 5, pp. 6829-6839, 2014.

[15] R. O. Scattergood and J. L. Routbort, "Velocity and Size Dependences of the Erosion Rate in Silicon," *Wear,* vol. 67, pp. 227-232, 1981.

[16] D. B. Marshall, B. R. Lawn and A. G. Evans, "Elastic/Plastic Indentation Damage in Ceramics: The Lateral Crack System," *Journal of the American Ceramic Society,* vol. 65, no. 11, pp. 561-566, 1982.

[17] S. M. Wiederhorn and B. R. Lawn, "Strength Degradation of Glass Impacted with Sharp Particles: I, Annealed Surfaces," *Journal of the American Ceramic Society,* vol. 62, no. 1-2, pp. 66-70, 1979.

[18] A. G. Evans, M. E. Gulden and M. Rosenblatt, "Impact Damage in Brittle Materials in the Elastic-Plastic Repsonse Regime," *Proceedings of the Royal Society of London. Series A,* vol. 361, pp. 343-365, 1978.

[19] S. Srinivasan and R. O. Scattergood, "R-Curve Effects in Solid Particle Erosion of Ceramics," *Wear,* vol. 142, no. 1, pp. 115-133, 1991.

[20] B. J. Hockey, S. M. Wiederhorn and H. Johnson, "Erosion of Brittle Materials by Solid Particle Impact.," in *Flaws and Testing. Fracture Mechanics of Ceramics*, vol. 3, R. C. Bradt, D. P. H. Hasselman and F. F. Lange, Eds., Boston, MA: Springer, 1978.

[21] J. Zhou and S. Bahadur, "Erosion Characteristics of Alumina Ceramics at High Temperatures," *Wear,* Vols. 181-183, no. 1, pp. 178-188, 1995.

[22] R. G. Wellman and C. Allen, "The Effects of Angle of Impact and Materials Properties on the Erosion Rates of Ceramics," *Wear,* Vols. 186-187, pp. 117-122, 1995.

[23] N. M. Barkoula and J. Karger-Kocsis, "Solid Particle Erosion of Unidirectional GF Reinforced EP Composites with Different Fiber/Matrix Adhesion," *Journal of Reinforced Plastics and Composites,* vol. 21, no. 15, pp. 1377-1388, 2002.

[24] U. S. Tewari, A. P. Harsha, A. M. Hager and K. Friedrich, "Solid Particle Erosion of Carbon Fibre-and Glass Fibre-Epoxy Composites," *Composites Science and Technology,* vol. 63, no. 3-4, pp. 549-557, 2003.

[25] A. Patnaik, A. Satapathy, N. Chand, N. M. Barkoula and S. Biswas, "Solid Particle Erosion Wear Characteristics of Fiber and Particulate Filled Polymer Composites: A Review," *Wear,* vol. 268, pp. 249-263, 2010.

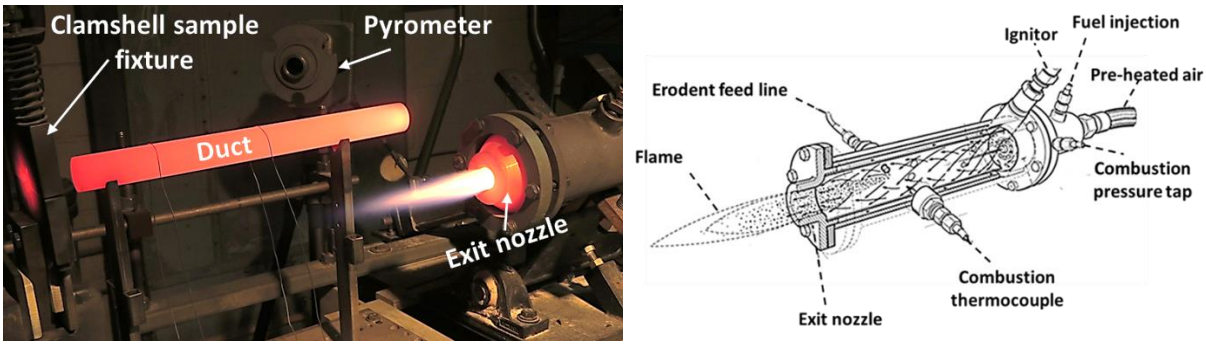

(a) **(b)**

Figure 1: Erosion burner rig configuration. (a) Burner rig exit nozzle, unattached duct, clamshell sample fixture, and pyrometer. (b) Schematic of the burner rig placed before the duct.

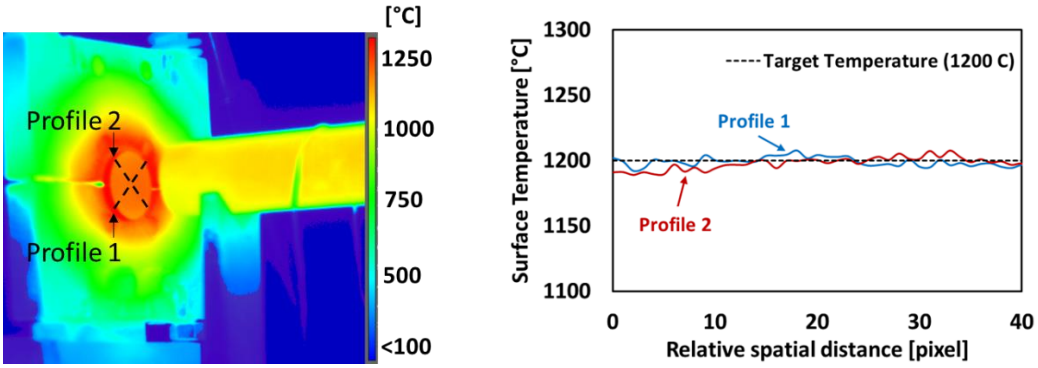

(a) **(b)**

Figure 2. Surface temperature distribution as measured using a FLIR A655sc. (a) Thermal image of sample heated to 1,200 °C. (b) Temperature profiles measured across the sample as shown in (a).

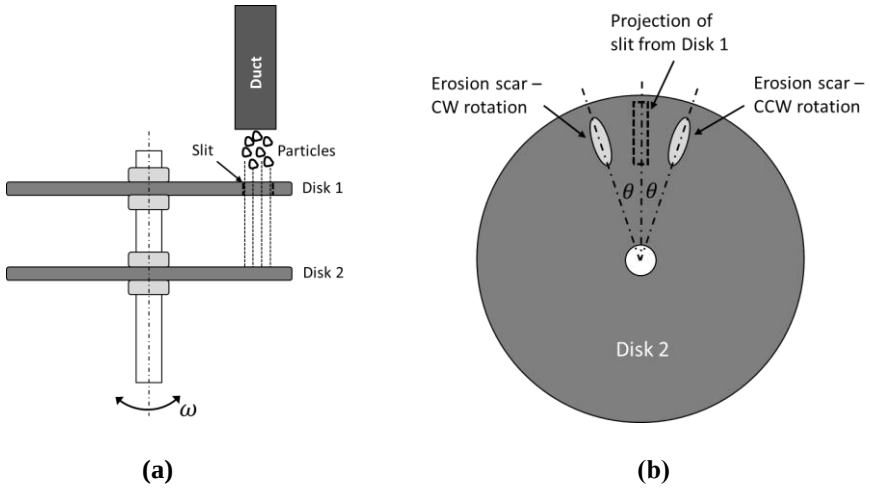

(a) **(b)**

Figure 3. Schematic of double disk velocimetry. (a) Top-down view. (b) Front view of Disk 2 after particle exposure. Clockwise (CW). Counterclockwise (CCW).

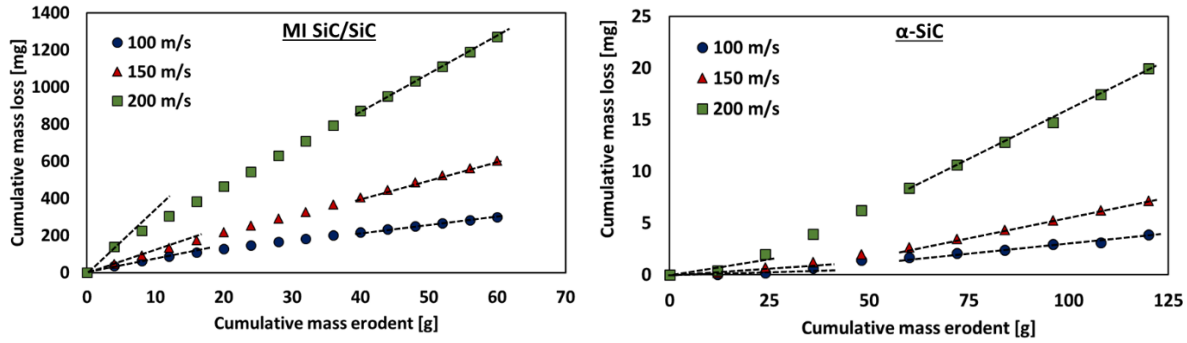

(a) **(b)**

Figure 4. Cumulative mass loss versus cumulative mass erodent curves at 90° particle impingement. (a) MI SiC/SiC. (b) α-SiC.

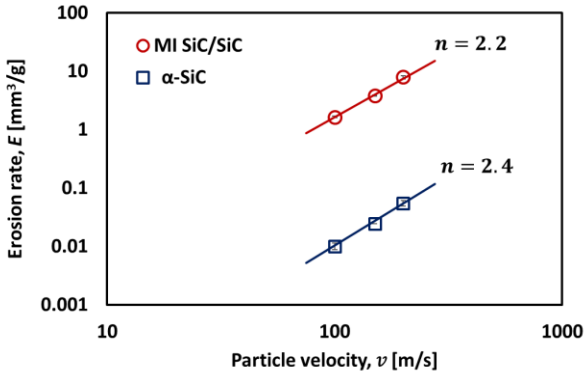

Figure 5. Steady-state erosion rate as a function of particle velocity for the MI SiC/SiC and α-SiC at 90° particle impingement and particle velocities of 100, 150, and 200 m/s. Note that the error bars (standard deviation) are contained within the symbols.

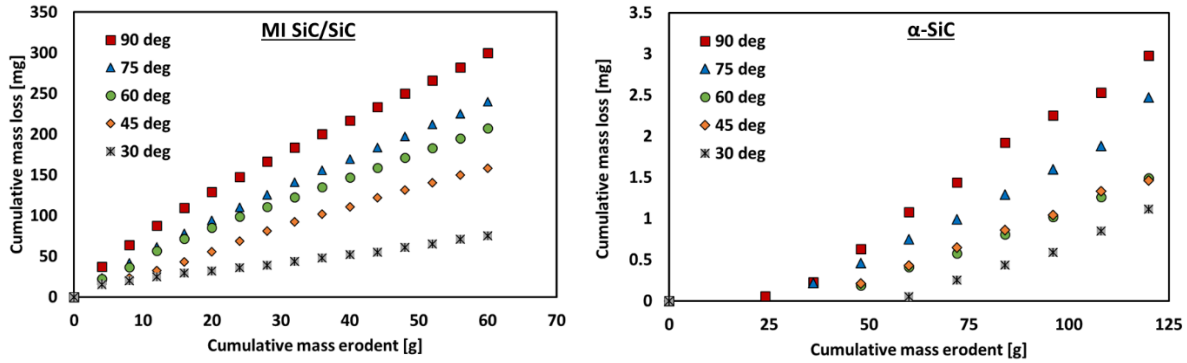

(a) **(b)**

Figure 6. Cumulative mass loss versus cumulative mass erodent curves for various impingement angles. (a) MI SiC/SiC. (b) α-SiC.

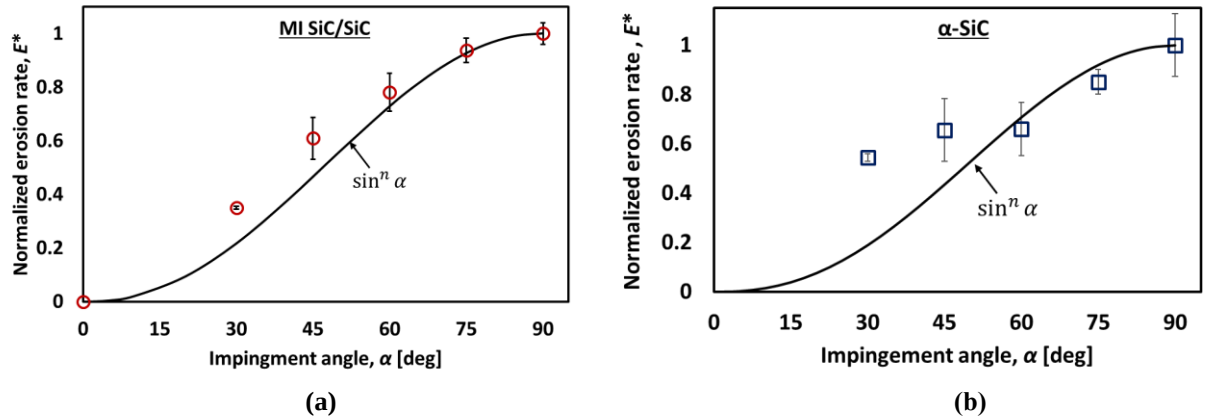

Figure 7. Normalized steady-state erosion rate, E^*, plotted as a function of impingement angle along with the $\sin^n \alpha$ law. (a) MI SiC/SiC ($n = 2.2$). (b) α-SiC ($n = 2.4$).

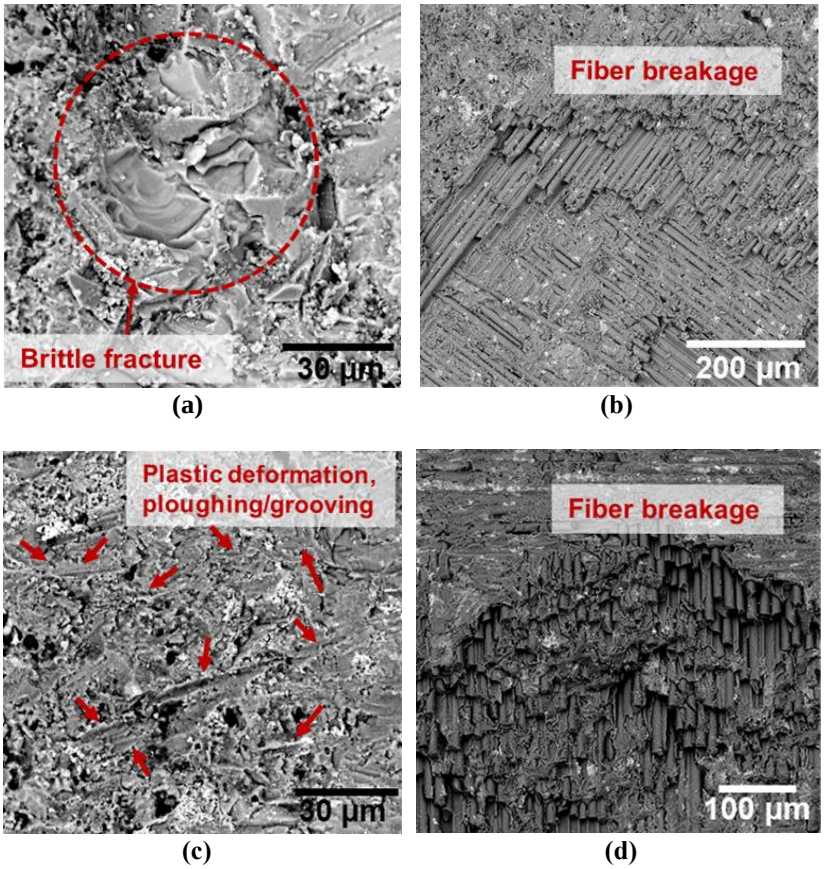

Figure 8. Steady-state erosion surfaces for the MI SiC/SiC at a particle velocity of 100 m/s. (a) 90° - matrix-rich region. (b) 90° - fiber-rich region. (c) 30° - matrix-rich region. (d) 30° - fiber-rich region.

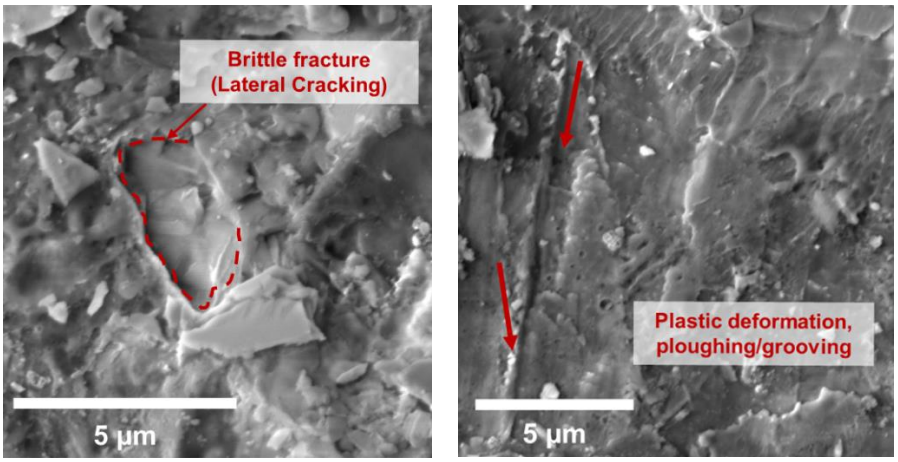

(a) (b)

Figure 9. Steady-state erosion surfaces for the α-SiC. (a) 90° at a particle velocity of 200 m/s. (b) 45° at a particle velocity of 100 m/s.

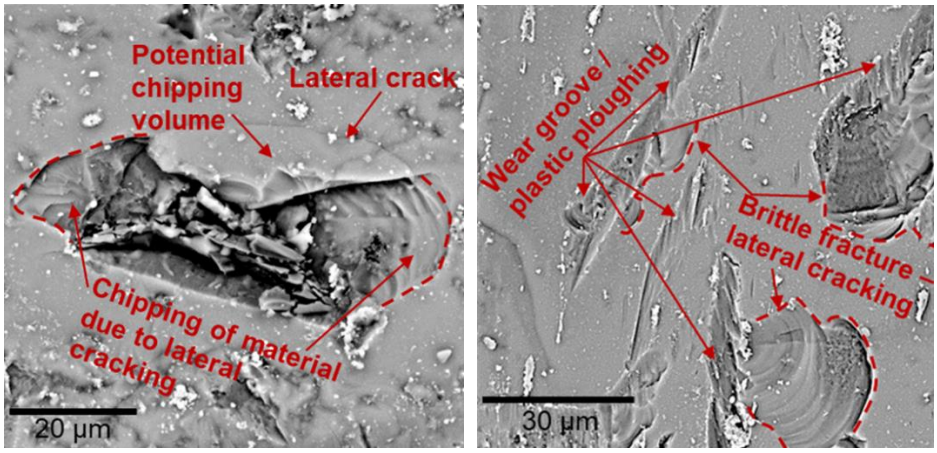

(a) (b)

Figure 10. Isolated impact damage events in a matrix-rich region in the MI SiC/SiC at a particle velocity of 100 m/s. (a) 90° impingement. (b) 30° impingement.

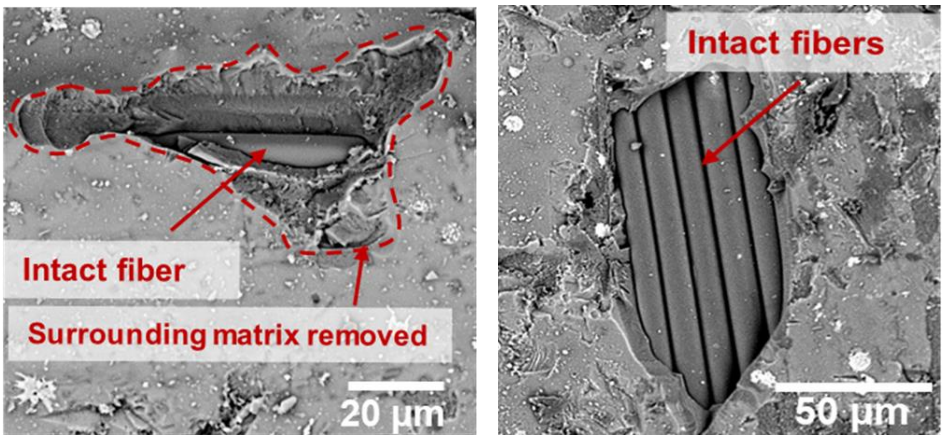

(a) (b)

Figure 11. Isolated impact damage events in the MI SiC/SiC at 90° and a particle velocity of 100 m/s resulting in ejected matrix material. (a) Surrounding matrix removed exposing a single, intact fiber. (b) Surrounding matrix removed exposing multiple fibers.